Research Square

Preprints are preliminary reports that have not undergone peer review.
They should not be considered conclusive, used to inform clinical practice,
or referenced by the media as validated information.

Experimental Investigation and Quantitative Pore Morphology of Aluminum Aerated Dense Concrete

Zerwal ASSOKA

laminezerwal1@gmail.com

Jomo Kenyatta University of Agriculture and Technology https://orcid.org/0009-0004-2700-9301

Research Article

Keywords: Aluminum-aerated dense concrete, foaming efficiency, digital image analysis, U-Net segmentation, pore morphology, mechanical degradation regimes

Posted Date: July 28th, 2026

DOI: https://doi.org/10.21203/rs.3.rs-10489916/v1

License: This work is licensed under a Creative Commons Attribution 4.0 International License.
Read Full License

Additional Declarations: The authors declare no competing interests.

Experimental Investigation and Quantitative Pore Morphology of Aluminum Aerated Dense Concrete

Zerwal Assoka[1*], John Nyiro Mwero[2], Nadjime Pindra[3], Kenji Kawai[4]

[1] *Department of Civil Engineering, Pan African University Institute for Basic Sciences, Technology and Innovation (PAUSTI), Hosted at the Jomo Kenyatta University of Agriculture and Technology (JKUAT), Nairobi, Kenya.*

[2] *Department of Civil and Construction Engineering, Technical University of Kenya (TUK), Nairobi, Kenya.*

[3] *Department of Mathematics, Faculty of Sciences, University of Lomé (UL), Lomé, Togo.*

[4] *Department of Civil and Environmental Engineering, Hiroshima University, Higashi-Hiroshima City, Japan.*

*Corresponding author. E-mail : laminezerwal1@gmail.com

Abstract

Chemically aerated dense concrete produced by aluminum powder addition exhibits a mechanical penalty that scalar porosity models cannot explain. In six mixes (0-5% aluminum by cement mass, w/c = 0.35), apparent porosity increased only from 3.24% to 6.18% while 28-day compressive strength collapsed by 56% (52.9 to 23.3 MPa); splitting tensile strength fell abruptly at 4% Al; and stoichiometric gas retention efficiency remained below 0.68% throughout. Three macroscopic anomalies emerged: a disproportionate 39% strength collapse at 1% Al, a non-monotonic tensile-to-compressive strength ratio peaking at 3% Al, and a porosity decrease at 4% Al coincident with a 27.4% tensile strength loss. Conventional strength-porosity models fit the data well (R^2 = 0.953-0.990) but cannot explain these anomalies, being scalar in porosity alone. U-Net segmentation of 60 polished cross-sections (12,718 characterized pores) resolves all three: the 1% Al collapse reflects a 7.3× pore-density increase combined with the lowest circularity in the series, multiplying Inglis stress-concentration sites; the f_t/f_c peak coincides with a local circularity maximum one dosage step earlier; and the 4% Al anomaly is confirmed as bubble coalescence by five convergent indicators. Results show that pore multiplication, not enlargement, governs porosity development, that gas retention rather than generation limits foaming efficiency, and that geometry-resolved descriptors not scalar porosity are required to explain and guide the design of aluminum-aerated dense concrete.

Keywords: *Aluminum-aerated dense concrete; foaming efficiency; digital image analysis; U-Net segmentation; pore morphology; mechanical degradation regimes.*

Introduction

Aerated concrete has attracted growing research interest for its reduced self-weight and improved thermal and acoustic insulation. Among methods for introducing air voids into a cementitious matrix, the chemical route using aluminum particles to generate hydrogen gas in situ via reaction with calcium hydroxide remains the most industrially established:

$$2Al + 3Ca(OH)_2 + 6H_2O \rightarrow 3CaO \cdot Al_2O_3 \cdot 6H_2O + 3H_2\uparrow \quad (1)$$

Most published work on aluminum-aerated systems targets lightweight formulations at high w/c ratios, where mechanical penalties scale predictably with porosity. Paikara & Gyawali (2023) reported a 58% compressive strength loss and 52% modulus reduction for only a 50% density reduction at 0.6% aluminum, confirming that even lightweight systems show disproportionate penalties relative to density reduction. How this disproportion behaves in a dense, high-strength matrix under ambient curing where paste stiffness and viscosity, not w/c ratio, govern gas retention remains uncharacterized.

A second gap concerns microstructural characterization. DIA of aerated and foam concretes has relied on global thresholding, typically Otsu's method (Chica et al., 2022; Chung et al., 2017), workable because low paste viscosity allows near-spherical bubble equilibrium before setting, producing a clear bimodal gray-level histogram. Dense matrices with w/c $\leq$ 0.40 behave differently: rapid rheological locking produces irregular pore geometries, and polished sections contain three to five overlapping spectral phases (pores, hydrated paste, unreacted cement, aggregate) for which no global threshold is stable. Convolutional segmentation resolves this ambiguity where thresholding fails: Bangaru et al. (2022) achieved 94.4% accuracy across four concrete phases via U-Net, and deep-learning segmentation has since extended to meso-structural

characterization of complex concrete systems (Chen et al., 2024). No such approach had been applied to dense, chemically aerated concrete under ambient curing.

A third limitation is interpretive rather than methodological. Established DIA-strength studies (Nambiar & Ramamurthy, 2007) relate air-void parameters to density and strength across mix series frameworks built to describe smooth trends, not to explain a single discontinuous feature: a disproportionate strength collapse at one dosage, a non-monotonic strength ratio, or a porosity decrease coincident with strength loss, as documented here. Such frameworks have no mechanism to resolve why these occur. This defines the present study's stance: each macroscopic anomaly is treated as a falsifiable, mechanistic question answered by geometry-resolved pore descriptors, not restated as a correlation.

This study integrates macroscopic characterization of six aluminum-aerated dense concrete mixes (0-5% Al, w/c = 0.35), porosity, density, compressive/tensile/flexural strength, gas retention efficiency, and strength-porosity modeling with U-Net-based digital image analysis of 60 polished cross-sections (12,718 characterized pores), testing whether pore number density, size distribution, and shape explain three macroscopic anomalies that scalar porosity models cannot.

Materials and Methods

Materials

Portland-pozzolanic cement CEM II/B-L 42.5 N (EN 197-1) was the sole binder; its chemical composition (Table 1) is from the same cement source characterized by Londe et al. (2025). Fine aggregate was natural river sand (d_{max} = 5 mm) and coarse aggregate was crushed granite (d_{max} = 14 mm); particle size distributions followed ASTM C136, verified against ASTM C33/C33M. Aggregate Crushing Value and Aggregate Impact Value assessed coarse aggregate soundness. Aluminum particles ($d_{max} \leq$ 2 mm, purity ≥ 98% Al), from mechanically ground foil, served as

generating agent. A polycarboxylate-based superplasticizer (Sika ViscoCrete 20HE, conforming ASTM C494/C494M was dosed at 1.0% by cement mass across all mixes. Mixing water was potable tap water.

Table 1. Chemical properties of CEMII 42.5 N (Londe et al., 2025)

Parameter	Abbreviation	Specification (wt %)	Result (wt %)
Calcium oxide	CaO	60-67	57.06
Silicon dioxide	SiO_2	17-24	24.42
Aluminum oxide	Al_2O_3	3-6	6.02
Ferric oxide	Fe_2O_3	0.5-3	3.75
Magnesium oxide	MgO	≤ 5.0	1.28
Sulphur trioxide	SO_3	≤ 3.5	2.66
Sodium oxide	Na_2O	-	0.84
Loss on ignition	LOI	≤ 5.0	4.19
Insoluble residue	I.R.	≤ 5.0	12.05
Chloride content	Cl^-	≤ 0.10	< 0.01

Concrete Mix Design and Specimen Preparation

Six mixes were designed using the Densified Mixture Design Algorithm (Koteng, 2013) with a constant water-to-cement ratio (w/c = 0.35) and a fixed superplasticizer dosage with aluminum particle content varied from 0-5% by cement mass in 1% increments (Table 2).

Table 2: Concrete mix proportions (per m³).

Mix ID	Cement (kg/m³)	w/c	Fine Aggregate (kg/m³)	Coarse Aggregate (kg/m³)	SP (kg/m³)	Al particle (kg/m³)	Al (% cem.)
00Al (Control)	523.0	0.35	791	885	5.23	0.00	0%
01Al	523.0	0.35	791	885	5.23	5.23	1%
02Al	523.0	0.35	791	885	5.23	10.46	2%
03Al	523.0	0.35	791	885	5.23	15.69	3%
04Al	523.0	0.35	791	885	5.23	20.92	4%
05Al	523.0	0.35	791	885	5.23	26.15	5%

Mixing followed a fixed sequence in a rotary drum mixer (water/superplasticizer, cement, fine aggregate, aluminum, coarse aggregate); gas bubble formation was visible within ~1 minute, with

visible volumetric expansion during casting (Figure 1), motivating the gas retention efficiency analysis presented later in this section.

(a) (b)

Figure 1: Onset of gas bubble formation and fresh concrete expansion

Fresh mixture was cast into 100×100×100 mm cubes (compression, water absorption), Ø100×200 mm cylinders (splitting tensile), and 100×100×350 mm beams (flexural); specimen counts are in Table 3. Specimens were demolded at 24 h and water-cured (20±2°C) until testing at 7, 14, and 28 days.

Table 3: Summary of specimen quantities per mix and test type.

Mix	Al (%)	Cubes (Compression)	Cubes (Water Absorption)	Cubes (Image Analysis)	Cylinders (Split tensile)	Beams (Flexural)	Total
M0	0	12	3	2	3	3	23
M1	1	12	3	2	3	3	23
M2	2	12	3	2	3	3	23
M3	3	12	3	2	3	3	23
M4	4	12	3	2	3	3	23
M5	5	12	3	2	3	3	23
Total		**72**	**18**	**12**	**18**	**18**	**138**

Testing Program

Apparent porosity and dry density were determined on cubic specimens (100 × 100 × 100 mm) by the water absorption method following ASTM C642 with three replicate measurements per mix. Compressive strength tests were conducted on a servo-hydraulic press at a loading rate of 0.5 MPa/s following (BS EN 12390-3). Splitting tensile strength was measured on cylindrical specimens at a loading rate of 0.04 MPa/s (ASTM C496/C496M), Flexural strength (modulus of rupture, MOR) was determined by three-point bending on prismatic beams (ASTM C78/C78M).

Statistical Analysis and Regression Models

One-way ANOVA ($\alpha = 0.05$) was performed for compressive and splitting tensile strength; coefficient of variation assessed repeatability. Strength-porosity relationships were fitted using the Ryshkewitch-Duckworth model, $f_c = f_0 \cdot exp(-b \cdot P)$ (2), and the power-law model, $f_c = a \cdot P^n$ (3), by non-linear least squares (R^2, RMSE, AIC for comparison). A unified model, $f_c(P, t) = A \cdot t^{\alpha} \cdot P^{\beta}$ (4), was fitted to all 18 mix×age combinations simultaneously; this fit is strictly descriptive within the tested porosity (3.2-6.2%) and age (7-28 d) ranges, with no claim of generalization beyond this mix family. Gas retention efficiency η was defined as $\eta = V_{pore,exp}/V_{H_2,theoretical} \times 100$ (5), where $V_{pore,exp} = P/100$ and $V_{H_2,theoretical}$ is computed from H_2 stoichiometry (Eq. 1) at 24.5 L/mol (25°C); this reflects gas retention within the matrix, not intrinsic reaction yield.

Pore Structure Imaging and Quantitative Digital Image Analysis

Ten cross-sections per mix (60 total; two dedicated cubes per mix, Z- and Y-sectioned) were cut and polished (120-grit). Images were acquired with a Google Pixel 8 Pro (50 MP), calibrated per-image from the known 100 mm specimen width (~0.05 mm detection limit). Segmentation used U-Net (Ronneberger et al., 2015), trained on 847 annotated pores, chosen over global thresholding

(Otsu, 1979) because the multi-phase gray-level histogram (aggregate, mortar, cement, pores) has no stable global threshold, and because circularity is quadratically sensitive to perimeter error, to which thresholding is prone at aggregate boundaries. Pores with ECD < 0.25 mm were excluded (Griffith argument: $f_t \approx 3.5\ MPa, KIC \approx 0.4\ MPa\sqrt{m}$, critical flaw ≈ 0.04 mm), retaining 12,718 pores (Figure 2).

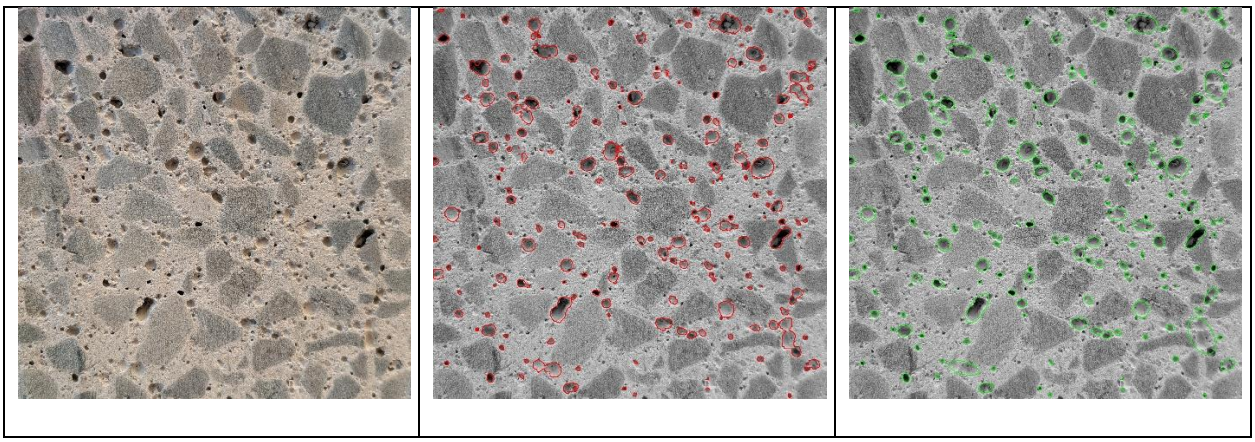

(a) (b) (c)

Figure 2: U-Net pore segmentation and ellipse fitting (Z-2% Al)

Descriptors: $d_e = \sqrt{(4Ap/\pi)}$, circularity $C = 4\pi A_p/{P_p}^2$, $AR = D_{minor}/D_{major}$ per pore; φ_Z, ρ, $H = \sigma(d_e)/\mu(d_e)$, $A = 1/\mu(C)$, $\bar{r} = \mu(d_e)/2$ per mix; $K_t = 1 + 2/\mu(AR)$ Inglis (1913). Segmentation performance was assessed visually and by comparing φ_Z against P_{ASTM}.

Results and Discussion

Aggregate Characterization

Particle size distributions confirmed compliance with ASTM C33/C33M grading requirements for both aggregates (Figure 3; FM = 2.83, dmax = 14 mm).

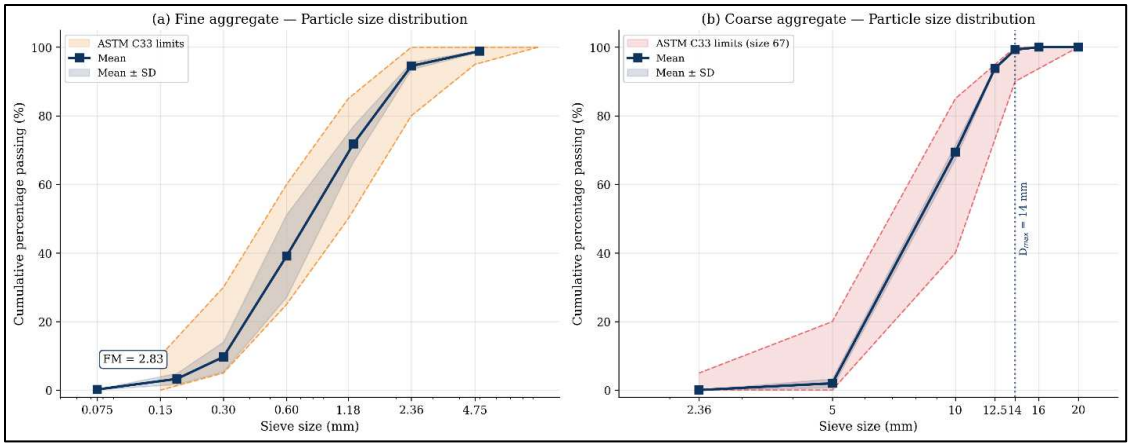

136

137 *Figure 3: Particle size distribution of (a) fine aggregate and (b) coarse aggregate with ASTM*

138 *C33 grading limits*

139 Physical and mechanical properties are summarized in Table 4. Coarse aggregate ACV (13.96%)

140 and AIV (5.20%) were well below the 30% and 20% structural limits, confirming that strength

141 reductions with increasing aluminum content are attributable to induced porosity rather than

142 aggregate weakness.

143 *Table 4: Physical and mechanical properties of fine and coarse aggregates*

Property	Coarse aggregates	Fine aggregates
Size range	5 - 14 mm	0-5 mm
Specific gravity on saturated dry Basic (g/cm^3)	2.54	2.36
Absolute dry specific gravity (g/cm^3)	2.44	2.23
Water absorption (% of dry weight)	3.92%	6.00 %
Fineness modulus	-	2.83
Aggregate bulk density	1.49	1.63
Aggregate crushing value (ACV)	13.96%	-
Aggregate impact value (AIV)	5.20%	-

144

145 **Qualitative Pore Structure Evolution**

146 Representative cross-sections at 0%, 2%, and 5% Al are shown in Figure 4.

147

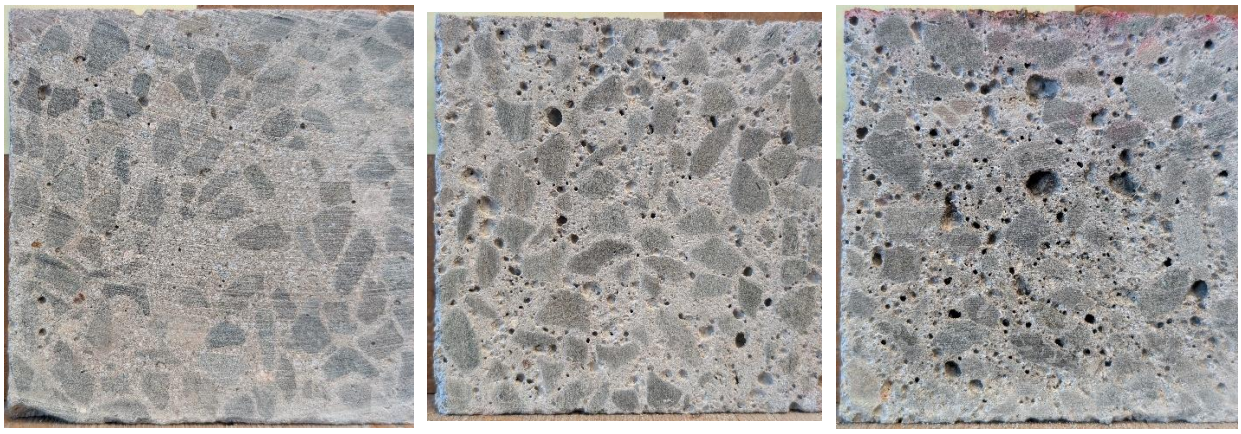

(a) (b) (c)

Figure 4: Representative cross-sections of concrete specimens containing 0%, 2%, and 5% aluminum particle, illustrating the qualitative evolution of the pore structure.

The control mix shows a dense, homogeneous structure with limited entrapped-air porosity; at 2% Al, discrete, uniformly distributed pores appear with the solid skeleton remaining continuous; at 5% Al, pores become larger and more frequent, with visible coalescence reducing the effective load-bearing cross-section. This qualitative progression is a preliminary observation, motivating the quantitative U-Net characterization developed later, which resolves the same progression via measured pore density, size, and shape and explains the mechanical anomalies discussed subsequently.

Porosity, Density, and Gas Retention Efficiency

Water absorption values (ASTM C642) ranged from 3.24±0.05% (control) to 6.18±0.02% (5% Al) (Figure5). A significant anomaly occurs at 4% Al: porosity decreases to 5.47% versus 5.83% at 3% Al (CV < 3.5% for all mixes, ruling out scatter). Dry density decreased from 2384±14 to 2184±18 kg/m³ (8.2% max reduction) modest relative to the compressive strength penalty documented in the Compressive Strength and Degradation Regimes section.

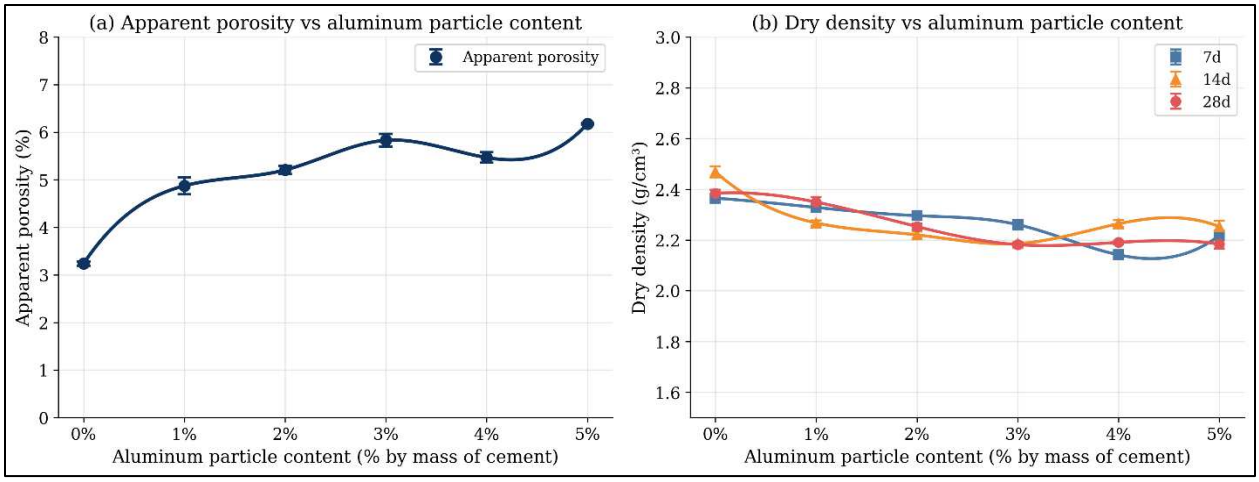

Figure 5: (a) Apparent porosity and (b) dry density versus aluminum content at all curing ages

Gas retention efficiency η (Eq. 5) ranged from 0.68% (1% Al) to 0.17% (5% Al), decreasing monotonically (Figure 6): most theoretically generated H_2 escapes rather than being retained as porosity.

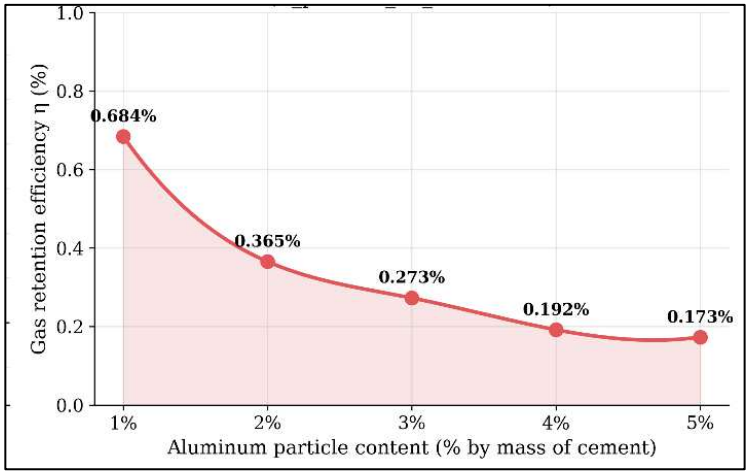

Figure 6: Stoichiometric gas retention efficiency η

Three mechanisms plausibly contribute: higher paste viscosity than conventional AAC (Narayanan & Ramamurthy, 2000) favors buoyancy-driven bubble rise over surface-tension stabilization as bubbles grow (Konan et al., 2023; Strybny et al., 2024); bubble coalescence promotes percolation and escape before stiffening, as documented by time-lapse CT in foam cements (Han et al., 2022); and some H_2 may remain entrapped under pressure, making η a conservative lower bound. This

decreasing trend directly relates to Regime 3, discussed in the Compressive Strength and Degradation Regimes section: beyond a critical dosage, added aluminum generates gas that is almost entirely lost. To the authors' knowledge, this is the first stoichiometric quantification of gas retention efficiency in aluminum-aerated dense concrete under ambient curing; the coalescence mechanism is confirmed directly from pore population data later in this section.

Compressive Strength and Degradation Regimes

Twenty-eight-day compressive strength decreased monotonically from 52.9±1.5 to 23.3±0.7 MPa (56% reduction) while density fell only 8.2% (Figure 7; ANOVA $F = 221.7$, $p < 0.001$, CV < 7%).

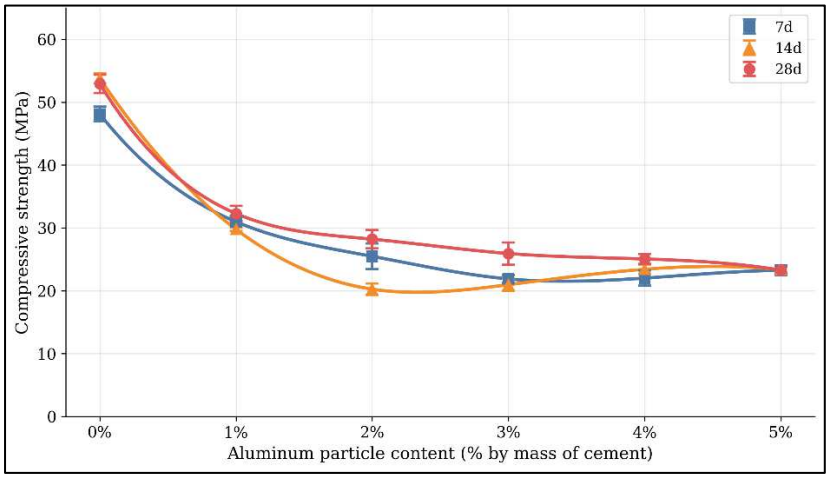

Figure 7: Compressive strength development

Degradation resolves into three regimes (Figure 8): Regime 1 (0-1% Al), a sharp -39% (-20.6 MPa) drop for only 1.63 percentage points of added porosity, the steepest degradation per unit dosage in the series, comparable to the disproportionate early-porosity penalties reported in fiber-reinforced concrete by Hu et al. (2025 ~17.5% peak-stress reduction between 2-4% porosity); Regime 2 (1-3% Al), slower weakening (-19.7% cumulative), consistent with Wang & Sun (2023); and Regime 3 (3-5% Al), near-saturation (-10.2% cumulative), consistent with Peng et al. (2024) for non-autoclaved sulfoaluminate-cement aerated concrete. These regimes are a macroscopic

characterization; the microstructural mechanism behind the Regime 1 collapse is identified once pore population data is introduced later.

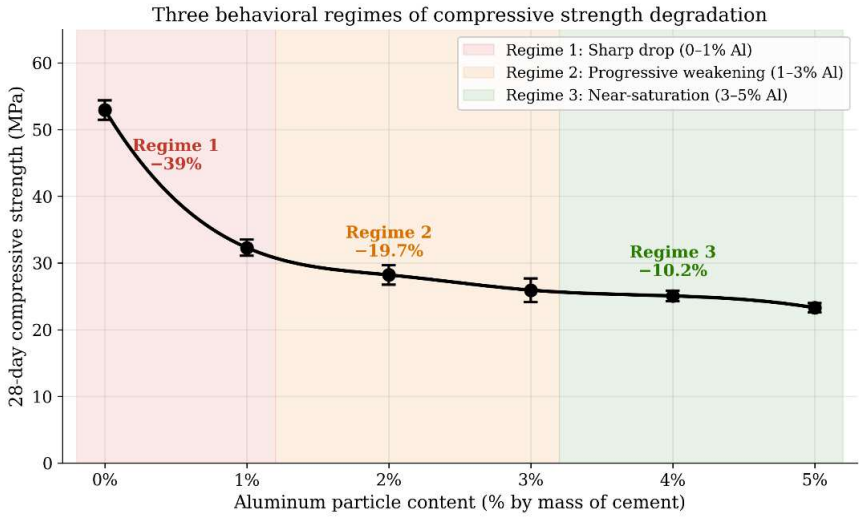

Figure 8: Three behavioral regimes of 28-day compressive strength degradation

Splitting Tensile Strength, Flexural Strength, and the f_t/f_c Ratio

Splitting tensile strength diverged sharply from compressive behavior (Figure 9a): a stable plateau for 0-3% Al (3.43-3.53 MPa) is followed by a drop to 2.49 MPa at 4% Al and 2.41 MPa at 5% Al (ANOVA $F = 33.6$, $p < 0.001$).

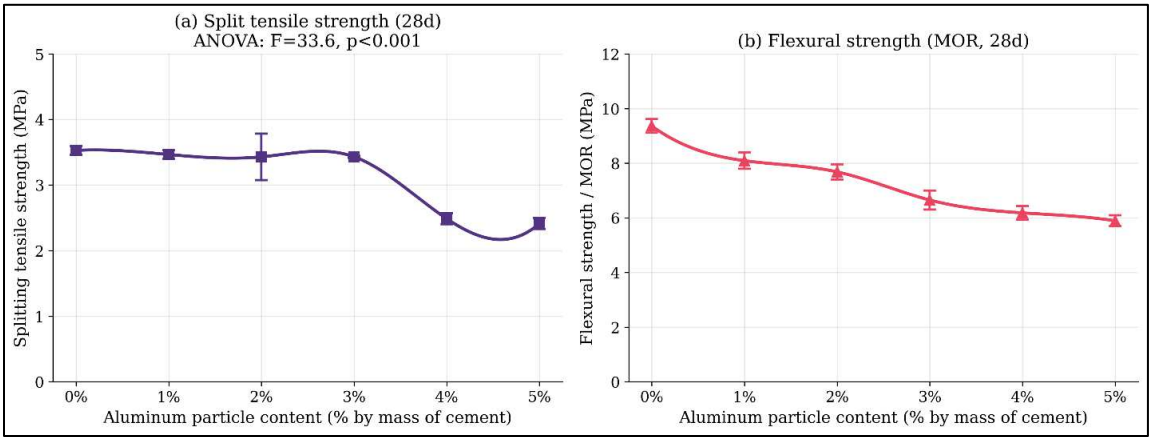

Figure 9: (a) 28-day splitting tensile strength with ANOVA results ($F = 33.6$, $p < 0.001$); (b) 28-day flexural strength (MOR). Error bars represent ±1 standard deviation.

The control f_t/f_c (0.067) matches values reported for high-strength, low-w/c concrete (Arioglu et al., 2006); f_t/f_c then rises to a peak of 0.132 at 3% Al before dropping to 0.099 at 4% Al and recovering to 0.104 at 5% Al (Figure 10), a non-monotonic evolution examined mechanistically later. Flexural strength decreased more uniformly (9.36±0.25 to 5.89±0.20 MPa, 37%, Figure 9b), without the f_t threshold behavior, consistent with a stress-gradient failure mode less sensitive to pore connectivity than the biaxial split-tensile state. These trends broadly match Shabbar et al. (2017), though the sharp 4% Al transition was not observed in their lower-dosage range (up to 1% Al). Compressive strength alone is thus insufficient to characterize this material's mechanical response.

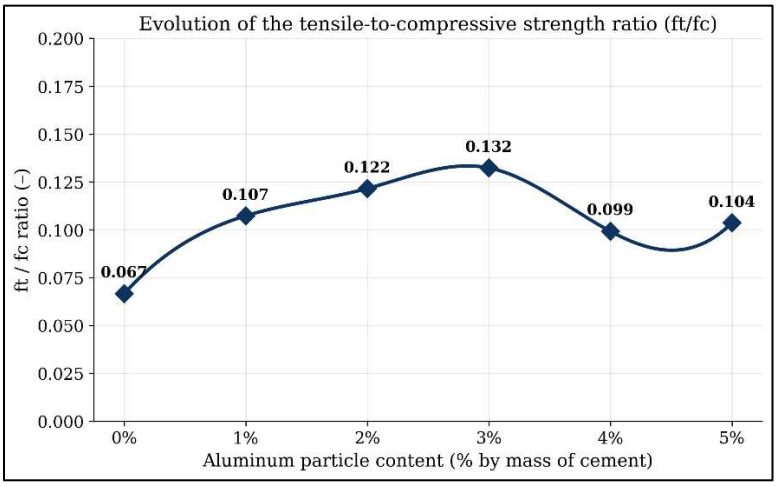

Figure 10: Evolution of the tensile-to-compressive strength ratio f_t/f_c with aluminum content

Compressive Strength-Porosity Relationships

R-D and power-law models were fitted at 7, 14, and 28 days (Table 5). Power-law consistently outperformed R-D (28d: R^2 = 0.990, RMSE = 1.018 MPa vs. R^2 = 0.984, RMSE = 1.277 MPa), consistent with Wang & Sun (2023) (Figure 11). A unified model, $f_c(P,t) = 217.22 \cdot t^{0.0657} \cdot P^{-1.3735}$ (R^2 = 0.953, RMSE = 2.258 MPa), was fitted across all 18 mix×age combinations.

Table 5: Model comparison summary

Age	Model	Param 1	Param 2	R^2	RMSE (MPa)	AIC
7d	R–D	f_0 = 124.16	b = 0.294	0.958	1.897	11.68
7d	Power-law	a = 215.89	n = −1.276	0.963	1.769	10.85 ✓
14d	R–D	f_0 = 170.52	b = 0.361	0.928	3.143	17.74
14d	Power-law	a = 335.26	n = −1.564	0.946	2.724	16.03 ✓
28d	R–D	f_0 = 137.35	b = 0.297	0.984	1.277	6.93
28d	Power-law	a = 240.26	n = −1.288	0.990	1.018	4.21 ✓

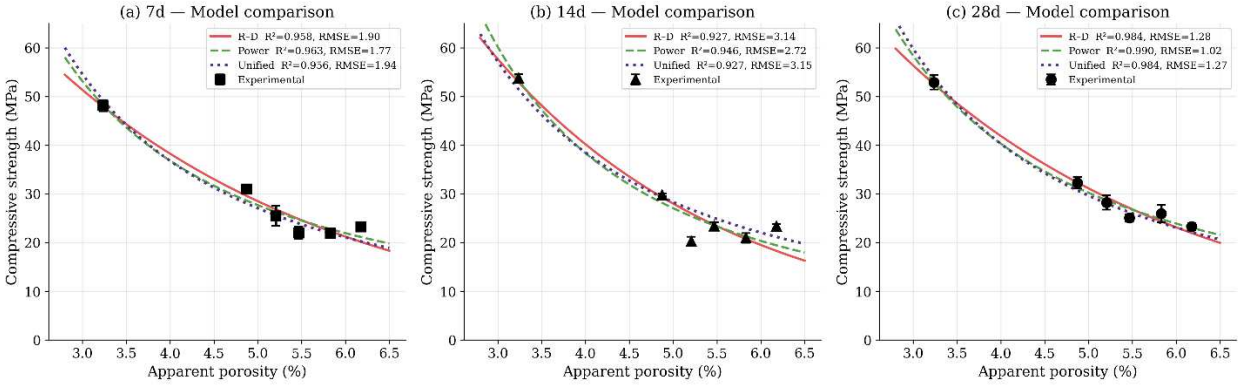

Figure 11: Strength-porosity relationships fitted by R-D and power-law models at (a) 7 days, (b) 14 days, and (c) 28 days of curing.

The small hydration exponent ($\alpha = 0.0657 \pm 0.033$) indicates modest strength gain beyond 7 days; the porosity exponent ($\beta = -1.374 \pm 0.072$) confirms steeper-than-linear decline (Figure 12). Residual analysis (Figure 13) showed no systematic age-dependent bias. Unlike the linear model of Tang Van et al. (2019, $R^2 = 0.815$), the present model captures non-linear porosity-hydration interaction; as stated in the Statistical Analysis and Regression Models section, this fit is descriptive within the tested range only, and generalization beyond this mix design would require independent validation.

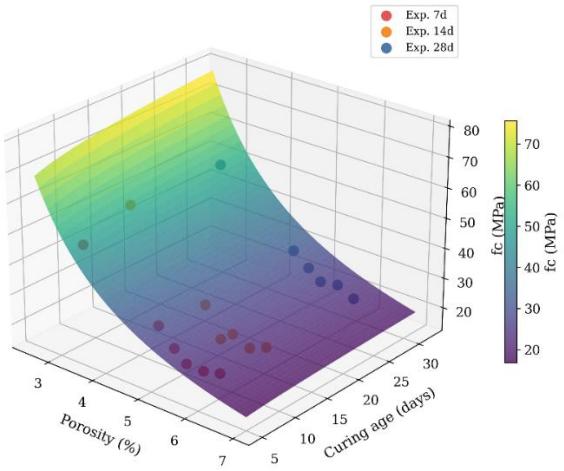

Figure 12: Predictive surface of the unified model $f_c(P,t) = 217.22 \cdot t^{0.0657} \cdot P^{-1.3735}$ across porosity (2.5 - 7%) and curing age (5 - 32 days)

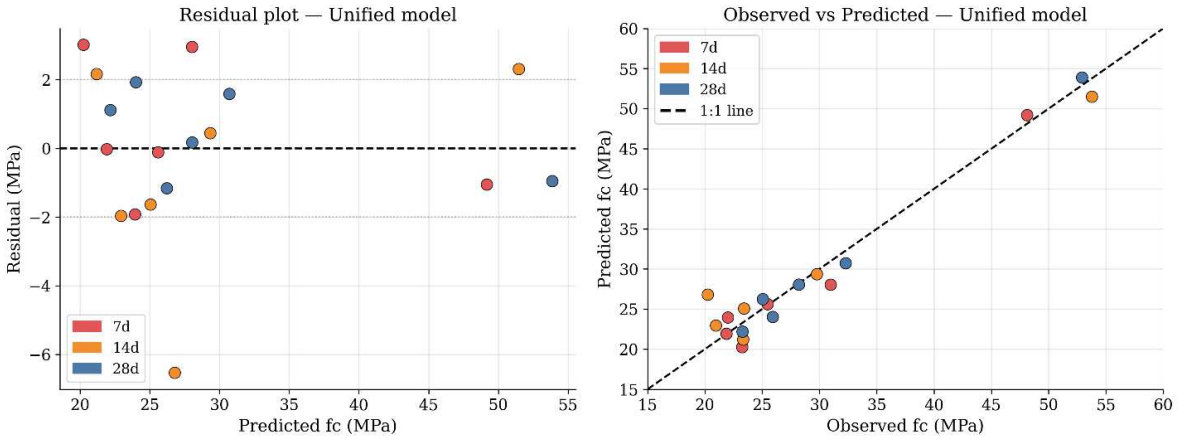

Figure 13: (a) Residual plot showing prediction errors; (b) observed versus predicted compressive strength

Pore Population and Area Fraction

Table 6 presents pore population statistics (60 sections, 10 per mix). Pore number density ρ shows an abrupt 7.3× step increase between 0% and 1% Al (0.00337 → 0.02467 pores/mm²), then increases more gradually, plateauing at 4-5% Al (ρ ≈ 0.034). φ_Z exceeds P_{ASTM} for all aluminum-containing mixes (ratio 1.05-1.49), consistent with known stereological overestimation of 3D void

fraction by 2D area for non-spherical pores (Underwood, 1970). The 4% Al mix shows the highest φ_Z (8.15%) despite P_{ASTM} being lower than at 3% Al, the first quantitative signature of the anomaly identified macroscopically in the Porosity, Density, and Gas Retention Efficiency section. For the control mix, φ_Z = 0.403% captures only the macro-pore fraction above the 0.25 mm threshold; its P_{ASTM} (3.24%) is primarily capillary/gel porosity invisible to DIA, a scope difference not affecting the aluminum-containing mixes (φ_Z/P_{ASTM} = 1.05-1.49).

Table 6: Pore population statistics from U-Net DIA (60 sections, 10 per mix)

Mix	Al (%)	N pores (Y+Z)	Images	ρ (pores/mm²)	φ_Z (%) transverse	P_{ASTM} (%) Mean ± SD	Ratio φ_Z/P
00Al	0	281	10	0.00337	0.403	3.24±0.05	0.124
01Al	1	2086	10	0.02467	6.192	4.87±0.17	1.272
02Al	2	2129	10	0.02538	5.691	5.21±0.09	1.093
03Al	3	2598	10	0.03160	6.394	5.83±0.13	1.097
04Al	4	2856	10	0.03417	8.154	5.47±0.11	1.490
05Al	5	2768	10	0.03388	6.463	6.18±0.02	1.046

φ_Z vs. P_{ASTM}: Mechanically Active vs. Total Porosity

Figure 14 compares φ_Z against P_{ASTM}. For the control mix, φ_Z (0.40%) is far below P_{ASTM} (3.24%, ratio 0.124): the 0.25 mm threshold excludes the capillary/gel porosity dominating this mix, so the comparison is not meaningful here. For aluminum-containing mixes, φ_Z consistently exceeds P_{ASTM} (ratio 1.05-1.49): DIA area fraction overestimates 3D void volume for non-spherical pores (Underwood, 1970), and P_{ASTM} captures only hydraulically connected volume while φ_Z measures total geometric area, their difference reflects the geometrically isolated pore fraction, growing with aluminum content. The Pearson correlation across all six mixes is r = 0.874 (p = 0.023; $P_{ASTM} = 0.341 \cdot \varphi_Z + 3.243$). The 4% Al mix shows the largest divergence (highest φ_Z, P_{ASTM} below the 3% Al value), examined mechanistically later.

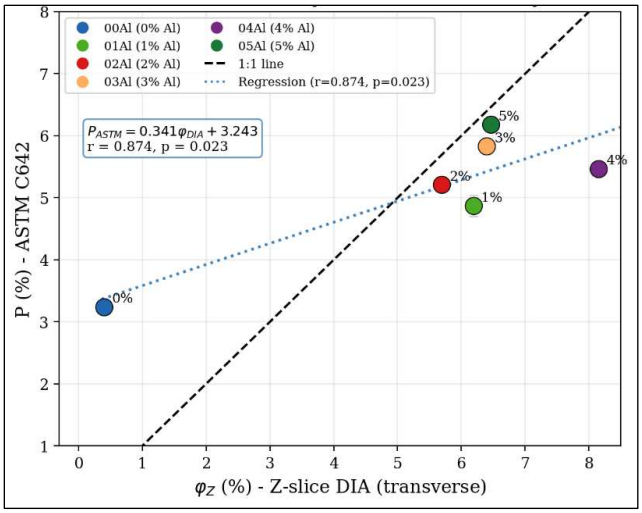

Figure 14: Z-slice DIA porosity vs ASTM C642 porosity

Pore Size Distribution

Table 7 presents ECD statistics. Mean ECD is near-invariant across 01Al-05Al (1.30-1.34 mm) despite a 4× increase in ρ, confirming pore multiplication rather than growth.

Table 7: Pore Equivalent Diameter (ECD) statistics

Mix	Al (%)	N pores	$\mu(d_e)$ mm	$\sigma(d_e)$ mm	d_{50} mm	d_{90} mm	$H = \sigma/\mu$	d_{max} mm
00Al	0	281	1.172	0.996	0.881	2.523	0.849[2]	5.913
01Al	1	2086	1.324	1.003	1.139	2.662	0.758	6.320
02Al	2	2129	1.342	0.978	1.152	2.646	0.729	5.755
03Al	3	2598	1.340	0.977	1.165	2.627	0.729	6.454
04Al	4	2856	1.304	1.048	1.094	2.639	0.804*	7.834*
05Al	5	2768	1.327	0.982	1.152	2.621	0.740	7.569

Three points follow. First, the 4% Al mix shows the lowest mean ECD among aluminum-containing mixes (1.304 mm) with the highest maximum (dmax = 7.83 mm) and highest H (0.804), a depressed mean with inflated maximum, indicative of coalesced large voids alongside newly nucleated small pores (Figure 15).

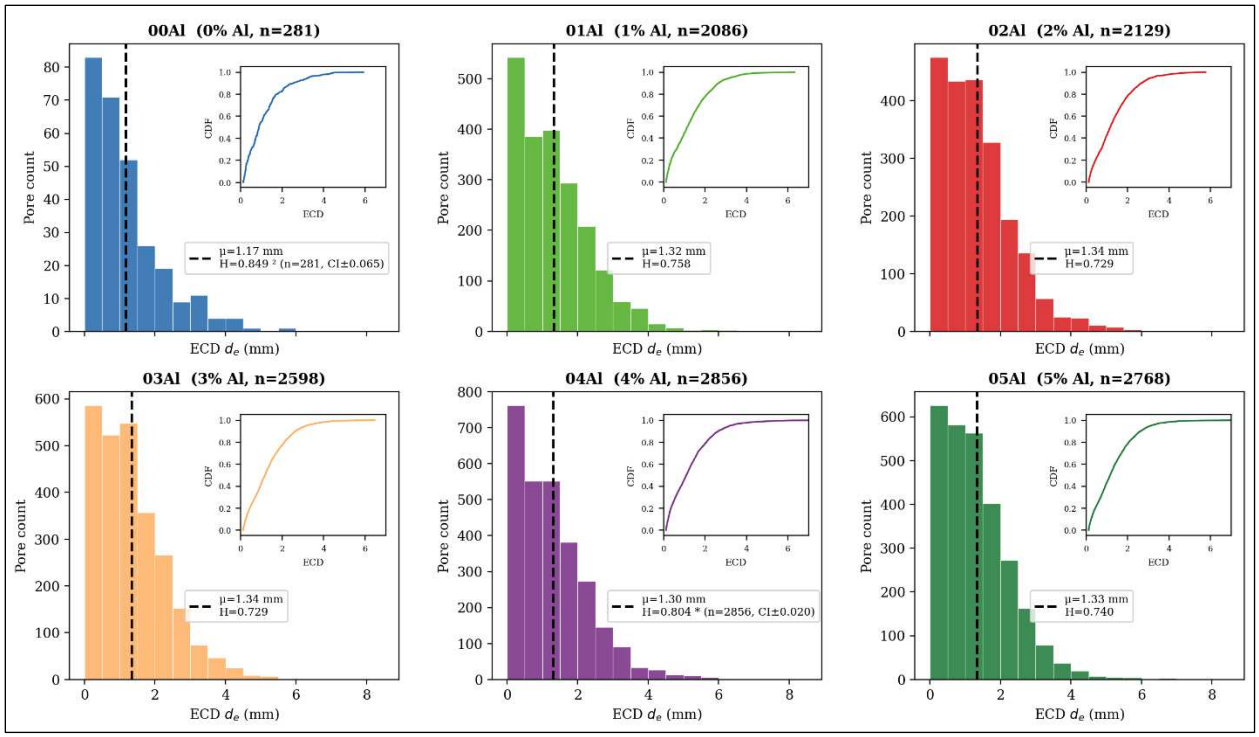

Figure 15: Pore ECD frequency distributions for all six mixes (bin width 0.5 mm)

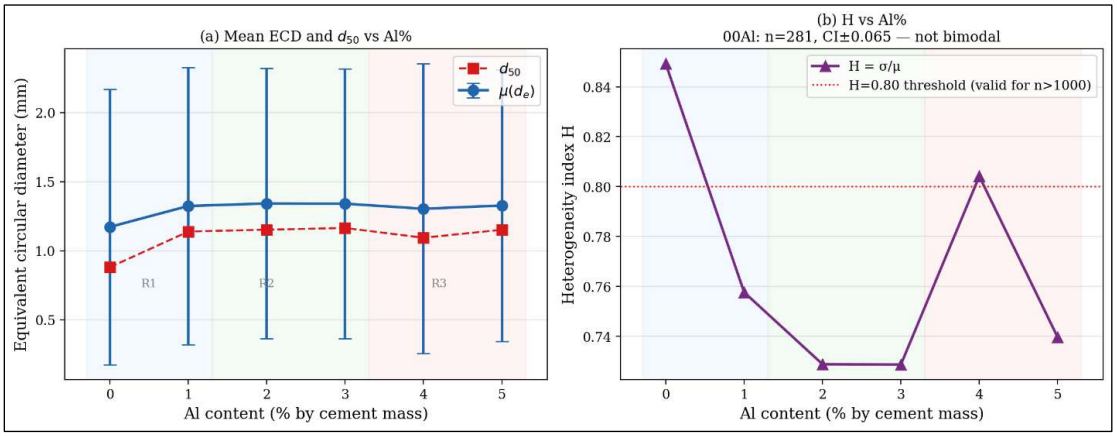

Figure 16: Mean ECD $\mu(d_e)$ and Heterogeneity index H vs Al content

Second, the control's H = 0.849 exceeds the 0.80 threshold but reflects sampling variance at low n (281 pores, bootstrap CI ±0.065) rather than genuine multimodality; H(04Al) = 0.804 (n = 2856, CI ±0.020) is unambiguously elevated relative to adjacent mixes (0.729, 0.740), with the multi-scale interpretation reliable only for n > 1000. Third, the step increase in μ(de) from 00Al (1.172

mm) to 01Al (1.324 mm), combined with lower circularity (Table 8), amplifies Inglis stress concentration at 1% Al (Figure 16).

Pore Shape Descriptors and Inglis Stress Concentration

Table 8 presents circularity and aspect ratio statistics with the Inglis (1913) stress concentration factor. $\mu(C)$ remains in a narrow range (0.684-0.707) across all mixes, indicating uniformly irregular pores regardless of dosage.

Table 8: Mean pore shape descriptors and Inglis (1913) stress concentration factors

Mix	**Al (%)**	**N pores**	$\boldsymbol{\mu(C)}$	$\boldsymbol{\sigma(C)}$	% $\boldsymbol{C \geq 0.70}$	$\boldsymbol{\mu(AR)}$	$\boldsymbol{\sigma(AR)}$	% $\boldsymbol{AR > 2}$	$\boldsymbol{K_t = 1 + 2/\mu(AR)}$ **(Inglis 1913)**
00Al	0	281	0.707	0.163	60.9	0.714	0.159	0.0	3.802
01Al	1	2086	0.684	0.163	54.9	0.694	0.163	0.0	3.882
02Al	2	2129	0.706	0.160	62.6	0.717	0.152	0.0	3.791
03Al	3	2598	0.690	0.163	57.2	0.700	0.155	0.0	3.858
04Al	4	2856	0.687	0.170	57.4	0.695	0.160	0.0	3.879
05Al	5	2768	0.694	0.163	58.8	0.695	0.155	0.0	3.878

The 1% Al mix has the lowest circularity (0.684), consistent with nucleation against partially set paste; $K_t = 1 + 2/\mu(AR) \approx 3.88$ at 1% Al, but since K_t is nearly constant across mixes (3.79-3.88), it is the 7.3× density increase described above in the Pore Population and Area Fraction section, not a shape anomaly, that amplifies stress concentration at this dosage. The 2-3% Al mixes show the highest circularity among aluminum-containing mixes (0.706, 0.690), a relative regularization relevant to the non-monotonic ft/fc peak examined later (Figure 17).

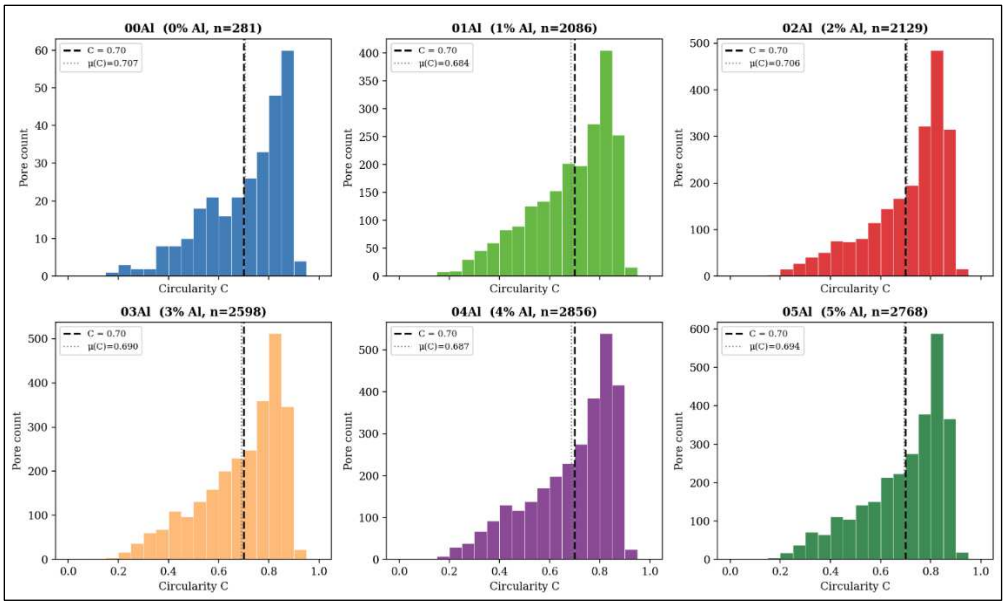

Figure 17: Circularity C frequency distributions for all six mixes (bin width 0.05)

No pore exceeded AR = 2, validating scalar shape descriptors without orientation correction; circularity vs. ECD for a representative sample is shown in Figure 18.

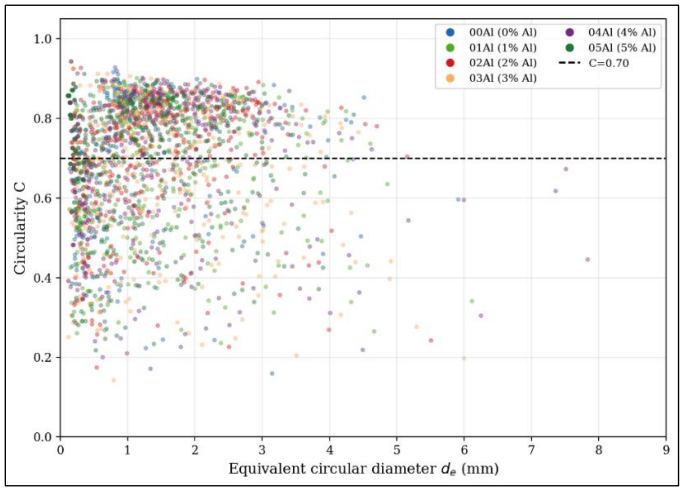

Figure 18: Individual pore circularity C vs. equivalent circular diameter ECD d_e

Pore Multiplication and Inglis Stress Concentration in Regime 1

Regime 1, introduced in the Compressive Strength and Degradation Regimes section, is a 39% strength collapse for only 1.63 percentage points of added porosity, the steepest degradation per unit dosage in the series explained by two DIA findings acting multiplicatively (Figure 19).

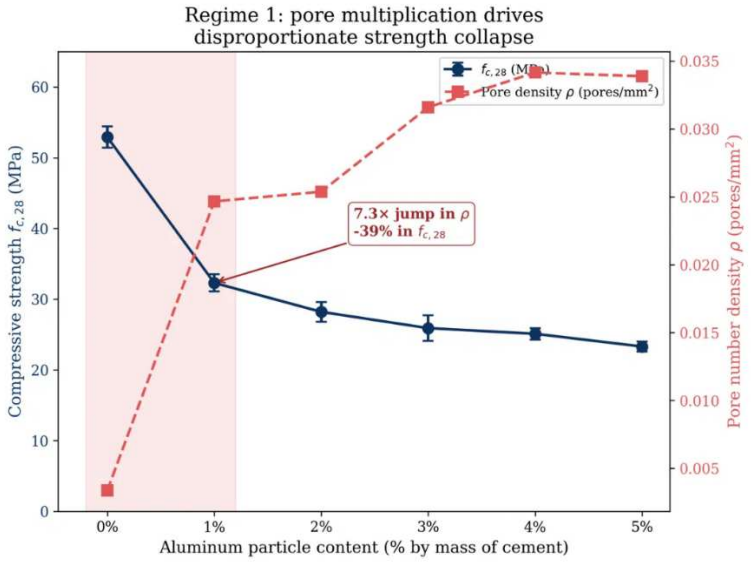

Figure 19: Compressive strength and pore number density as a function of aluminum

First, the 7.3× pore density increase at 1% Al (Table 6) reflects simultaneous nucleation of many small, irregular bubbles in a narrow rheological window before stiffening. Second, 1% Al pores show the series' lowest circularity (μ(C) = 0.684), giving $K_t = 1 + 2/\mu(AR) \approx 3.88$. Since K_t is nearly constant across mixes (3.79-3.88), the mechanically relevant quantity is the number of Kt-bearing sites per unit area, which increases 7.3× at this dosage raising the probability that at least one site locally exceeds matrix tensile strength and triggers fracture at a lower load than a scalar porosity model predicts. This reframes Regime 1 as a nucleation-density effect: strength loss is coupled to pore-density increase weighted by local flaw-exceedance probability, not simply proportional to porosity, when density changes abruptly while mean pore size remains constant (Table 7).

Circularity and the Non-Monotonic Evolution of the Tensile-Compressive Strength

The f_t/f_c ratio peaks at 3% Al (0.132) and collapses at 4% Al (0.099, as reported in the Splitting Tensile Strength, Flexural Strength, and the f_t/f_c Ratio section) because compressive and tensile failure operate at different length scales within the same pore population (Figure 20).

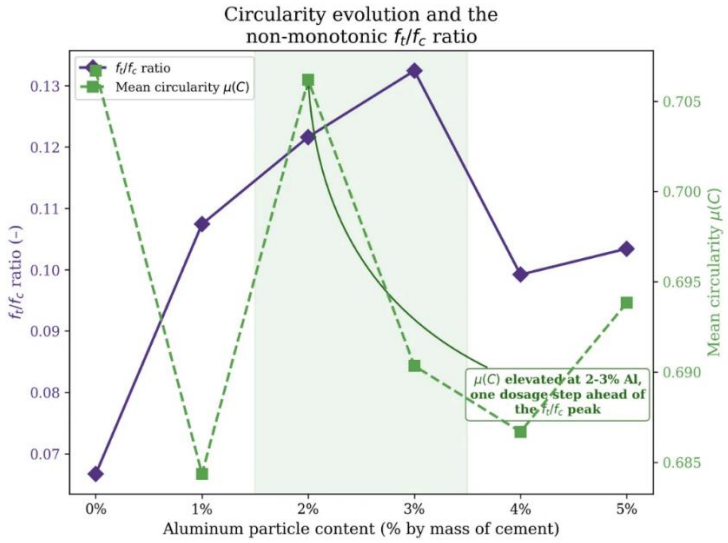

Figure 20: Splitting tensile-to-compressive strength ratio (f_t/f_c) and mean pore circularity as a function of aluminum content

Compressive failure involves distributed microcracking sensitive to mean-field properties (φ_Z, $\mu(C)$), degrading roughly monotonically; splitting tensile failure is governed by the single most critical pore, setting $KI \propto K_t \cdot \sigma \cdot \sqrt{r}$. Mean circularity peaks among aluminum-containing mixes at 2% Al (0.706), remaining elevated at 3% (0.690) one dosage step ahead of the f_t/f_c peak, preserving f_t relative to f_c before the 4% Al pore-population shift reverses the effect. At 4% Al, coalesced pores up to 7.83 mm (vs. 6.45 mm at 3% Al) increase KI by ~10%, sufficient to collapse f_t, while f_c drops only 3.1% over the same step reflecting mean-field compression's relative insensitivity to a single pore outlier, unlike diametral tension.

The control mix's high circularity (0.707) despite its low f_t/f_c (0.067) is not contradictory: at 0% Al, pore density is two orders of magnitude lower (Table 6), so pores are not the critical-flaw population; the low ft/fc instead reflects the known decrease of this ratio with matrix strength in dense, low-w/c concrete (Arioglu et al., 2006), independent of pore geometry. The circularity mechanism is thus scoped to the aluminum-containing mixes, where induced pores dominate the microstructure.

Convergent Evidence for Bubble Coalescence at 4% Aluminum

The coincident porosity dip and 27.4% tensile strength loss at 4% Al (established earlier in this Results and Discussion section) is confirmed as bubble coalescence by five convergent DIA signatures (Figure 21): the highest φ_Z (8.15%) despite lower P_{ASTM} as shown above; the largest maximum pore diameter (7.83 mm, 5.9× mean ECD); the lowest mean ECD among aluminum-containing mixes combined with the highest maximum, a bimodal fingerprint of merged large voids alongside newly nucleated small pores; the highest heterogeneity index (H = 0.804, CI ±0.020) relative to adjacent mixes (0.729, 0.740); and the lowest mean circularity (0.687) with highest spread (σ = 0.170), consistent with dumbbell-shaped coalesced voids.

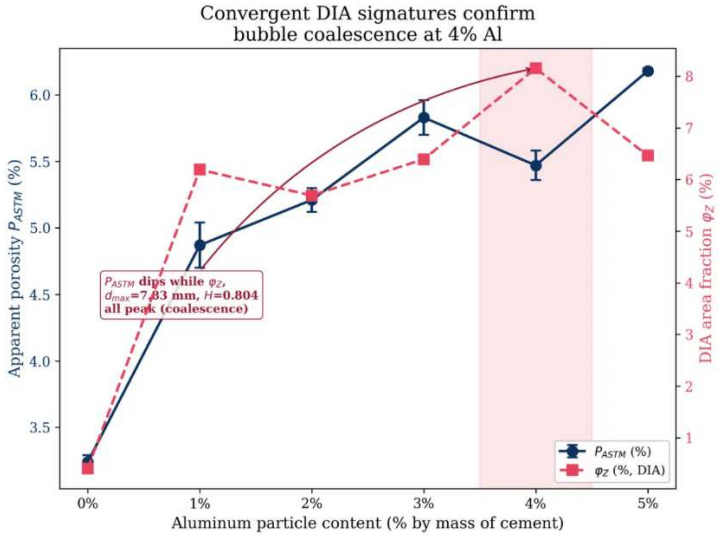

Figure 21: *Apparent porosity (P_{ASTM}) and DIA area fraction (φ_Z) as a function of aluminum content,*

Together, these indicators point to a small number of large merged voids alongside newly nucleated small pores explaining both the tensile collapse and porosity decrease, and substantiating the coalescence-driven gas-escape mechanism proposed in earlier for the low, dosage-decreasing η.

Limitations

Some limitations are acknowledged. Morphological descriptors derive from 2D sections; 3D connectivity, tortuosity, and percolation require dedicated reconstruction beyond this study's scope. Mix-level trends rest on n = 6; while within-image resolution is high (10 sections × 200-400 pores per mix), the anomaly resolutions rest on six data points per descriptor. The 0.25 mm ECD threshold, motivated by a Griffith argument, excludes fine capillary/gel porosity (DIA captures only ~12% of ASTM porosity for the control mix) appropriate for macro-crack mechanisms here, but requiring revision for durability applications. Characterization used two dedicated cubes per mix; inter-specimen variability beyond these was not directly quantified. The unified strength-porosity model described above is calibrated on 18 points from a single mix-design family; its R^2 reflects within-sample fit, not predictive generalization to other mix designs or aluminum sources.

Conclusion

This study integrated macroscopic characterization with U-Net-based digital image analysis to explain, not merely describe, the mechanical response of aluminum-powder aerated dense concrete (0-5% Al, w/c = 0.35) under ambient curing.

Apparent porosity increased from 3.24% to 6.18% while dry density fell only 8.2%, yet 28-day compressive strength dropped 56% (ANOVA $F = 221.7$, $p < 0.001$) the central macroscopic finding. Porosity increase is driven by pore multiplication, not enlargement: mean equivalent diameter remained near-constant (1.30-1.34 mm) across 1-5% Al while pore density increased four-fold.

Three degradation regimes were identified. The disproportionate Regime 1 collapse (39% loss for 1.63 percentage points of porosity) is explained by a 7.3× pore-density increase combined with the

lowest circularity in the series, multiplying Inglis stress-concentration sites rather than reflecting a shape anomaly. The non-monotonic f_t/f_c peak at 3% Al is explained by a circularity maximum at 2-3% Al reducing mode-I stress intensity one dosage step ahead of the peak. The coincident porosity dip and 27.4% tensile strength loss at 4% Al is confirmed as bubble coalescence by five convergent indicators, area fraction, maximum and mean pore diameter, heterogeneity index, and circularity, each individually inconclusive but collectively definitive.

Gas retention efficiency η remained between 0.17% and 0.68%, decreasing monotonically: gas retention, not generation, governs porosity development in this dense matrix, with coalescence at 4% Al directly implicated.

Conventional strength-porosity models, Ryshkewitch-Duckworth, power-law, and a unified model $f_c(P,t) = 217.22 \cdot t^{0.0657} \cdot P^{-1.3735}$ (R^2 = 0.953), fit well within the tested range and remain useful design tools there, but are not claimed to generalize beyond this mix design; they complement, rather than substitute for, the mechanistic account provided by microstructural analysis.

These results show that geometry-resolved descriptors, pore number density, size distribution, and circularity rather than scalar porosity alone, are necessary to explain and guide the design of aluminum-aerated dense concrete, and that dosages above 1% Al produce disproportionate penalties that must be weighed against the modest density reduction achieved.

Data Availability Statement

Some or all data, models, or code generated or used during the study are available from the corresponding author upon reasonable request.

Acknowledgments

The first author gratefully acknowledges the doctoral scholarship provided by the Pan African University Institute for Basic Sciences, Technology and Innovation (PAUSTI) in support of this research.

Notation

The following symbols are used in this paper:

A = amplitude parameter (unified strength-porosity model); AR = pore aspect ratio; b = sensitivity parameter (Ryshkewitch-Duckworth model); C = pore circularity; d_e = pore equivalent circular diameter; f_0 = theoretical strength at zero porosity; f_c = compressive strength; f_r = flexural strength (modulus of rupture); f_t = splitting tensile strength; H = heterogeneity index ($\sigma(d_e)/\mu(d_e)$); K_t = Inglis stress concentration factor; n = power-law exponent; N = number of pores; P = apparent porosity; P_{ASTM} = ASTM C642 apparent porosity; t = curing age; α, β = fitting exponents (unified model); η = stoichiometric gas retention efficiency; $\mu(\cdot)$, $\sigma(\cdot)$ = mean and standard deviation of a descriptor; φ_Z = Z-slice DIA area fraction.

References

Arioglu, N., Canan Girgin, Z., & Arioglu, E. (2006). Evaluation of ratio between splitting tensile strength and compressive strength for concretes up to 120 MPa and its application in strength criterion. *ACI Materials Journal*, *103*(1), 18–24. https://doi.org/10.14359/15123

ASTM C33/C33M. (2023, August 17). *Standard Specification for Concrete Aggregates*. https://store.astm.org/c0033_c0033m-18.html

ASTM C78/C78M-21. (2021). *Standard Test Method for Flexural Strength of Concrete (Using Simple Beam with Third-Point Loading)*. https://doi.org/10.1520/C0078_C0078M-21

ASTM C136-06. (2015, February 11). *Standard Test Method for Sieve Analysis of Fine and Coarse Aggregates*. https://store.astm.org/c0136-06.html

ASTM C494/C494M. (2020). *Standard Specification for Chemical Admixtures for Concrete*. https://store.astm.org/c0494_c0494m-17.html

ASTM C496/C496M-17. (2017). *Standard Test Method for Splitting Tensile Strength of Cylindrical Concrete Specimens*. https://doi.org/10.1520/C0496_C0496M-17

ASTM C642-21. (2021). *Test Method for Density, Absorption, and Voids in Hardened Concrete*. https://doi.org/10.1520/C0642-21

Bangaru, S. S., Wang, C., Zhou, X., & Hassan, M. (2022). Scanning electron microscopy (SEM) image segmentation for microstructure analysis of concrete using U-net convolutional neural network. *Automation in Construction*, *144*, 104602. https://doi.org/10.1016/J.AUTCON. 2022.104602

BS EN 12390-3. (2019). *Testing Hardened Concrete Compressive Strength of Test Specimens*. https://www.scirp.org/reference/referencespapers?referenceid=3765943

Chen, D., Li, Y., Tao, J., Li, Y., Zhang, S., Shan, X., Wang, T., Qiao, Z., Zhao, R., Fan, X., & Zhou, Z. (2024). Deep learning-based segmentation model for permeable concrete meso-structures. *Computer-Aided Civil and Infrastructure Engineering*, *39*(23), 3626–3645. https://doi.org/10.1111/mice.13300

Chica, L., Mera, C., Sepúlveda-Cano, L. M., & Alzate, A. (2022). Porosity estimation and pore structure characterization of foamed cement paste using non-specialized image digital processing. *Materials and Structures/Materiaux et Constructions*, *55*(7). https://doi.org/10.1617/s11527-022-02031-6

Chung, S. Y., Lehmann, C., Elrahman, M. A., & Stephan, D. (2017). Pore Characteristics and Their Effects on the Material Properties of Foamed Concrete Evaluated Using Micro-CT Images and Numerical Approaches. *Applied Sciences 2017, Vol. 7, Page 550*, *7*(6), 550. https://doi.org/10.3390/APP7060550

EN 197-1. (2000). *Cement - Part 1: Composition, specifications and conformity criteria for common*. https://standards.iteh.ai/catalog/standards/cen/00e43d7f-2f22-4b27-84dc-46026c47bfe3/en-197-1-2000?srsltid=AfmBOopHJOWkvHCWZok-6Mhm1i2GyKY7prubMQoEYA98f1SspOOGrXzs

Han, W. J., Park, J., Cha, W., Lee, J. S., & Santamarina, J. C. (2022). Pore topology, volume expansion and pressure development in chemically-induced foam cements. *Scientific Reports*, *12*(1), 16690. https://doi.org/10.1038/S41598-022-21128-0

Hu, A., Du, X., Wang, F., Li, J., Zhang, T., & Li, Y. (2025). Study on Damage Mechanism of Fiber Concrete with Initial Pores. *Materials 2025, Vol. 18, Page 916*, *18*(5), 916. https://doi.org/10.3390/MA18050916

Inglis, C. E. (1913). Stresses in a plate due to the presence of cracks and sharp corners. *Transactions of the Institute of Naval Architects*, *55*, 219–230.

Konan, N. A., Rosenbaum, E., & Massoudi, M. (2023). Motion of Air Bubbles in a Cement Slurry. *Materials 2023, Vol. 16, Page 6433*, *16*(19), 6433. https://doi.org/10.3390/MA16196433

Koteng, D. O. (2013, May). *The 20th Engineers' International Conference: Concrete use for sustainable development*.

Londe, G. H. M., Mwero, J. N., Kanali, C., & Abuodha, S. O. (2025). Strength, Water Porosity and Sulfuric Acid Performance of Coconut Fiber Reinforced High-Strength Concrete. *Civil Engineering Journal (Iran)*, *11*(4), 1672–1693. https://doi.org/10.28991/CEJ-2025-011-04-023

Nambiar, E. K. K., & Ramamurthy, K. (2007). Air-void characterisation of foam concrete. *Cement and Concrete Research*, *37*(2), 221–230. https://doi.org/10.1016/j.cemconres.2006.10.009

Narayanan, N., & Ramamurthy, K. (2000). Structure and properties of aerated concrete: A review. *Cement and Concrete Composites*, *22*(5), 321–329. https://doi.org/10.1016/S0958-9465(00)00016-0

Otsu, N. (1979). Threshold Selection Method From Gray-Level Histograms. *IEEE Trans Syst Man Cybern*, *SMC-9*(1), 62–66. https://doi.org/10.1109/tsmc.1979.4310076

Paikara, R. K., & Gyawali, T. R. (2023). Influence of aluminum powder content and powder-to-sand ratio on the physical and mechanical properties of aerated lightweight mortar. *Cleaner Materials*, *10*, 100213. https://doi.org/10.1016/J.CLEMA.2023.100213

Peng, F., Chen, C., Jiu, S., Song, Q., & Chen, Y. (2024). Preparation and Characterization of Novel Sulfoaluminate-Cement-Based Nonautoclaved Aerated Concrete. *Materials 2024, Vol. 17, Page 836*, *17*(4), 836. https://doi.org/10.3390/MA17040836

Ronneberger, O., Fischer, P., & Brox, T. (2015). U-Net: Convolutional Networks for Biomedical Image Segmentation. *Lecture Notes in Computer Science (Including Subseries Lecture Notes in Artificial Intelligence and Lecture Notes in Bioinformatics)*, *9351*, 234–241. https://doi.org/10.1007/978-3-319-24574-4_28

Shabbar, R., Nedwell, P., & Wu, Z. (2017). Mechanical properties of lightweight aerated concrete with different aluminium powder content. *MATEC Web of Conferences*, *120*, 02010. https://doi.org/10.1051/MATECCONF/201712002010

Strybny, B., Link, J., Coenen, M., Vidal, V., Zuber, M., Schack, T., & Haist, M. (2024). Mechanisms of air bubble rise in cement suspensions studied by X-ray analysis. *Construction and Building Materials*, *457*, 139330. https://doi.org/10.1016/J.CONBUILDMAT.2024.139330

Tang Van, L., Vu Kim, D., Ngo Xuan, H., Vu Dinh, T., Bulgakov, B., & Bazhenova, S. (2019). Effect of Aluminium Powder on Light-weight Aerated Concrete Properties. *E3S Web of Conferences*, *97*. https://doi.org/10.1051/e3sconf/20199702005

Underwood, E. E. (1970). Quantitative Stereology. In Addison-Wesley Publishing Company (Ed.), *Addison-Wesley, MA, CA, London*. https://books.google.com/books/about/Quantitative_Stereology.html?hl=fr&id=Epg1AAAAIAAJ

Wang, F., & Sun, C. (2023). Effect of pore structure on compressive strength and permeability of planting recycled concrete. *Construction and Building Materials*, *394*, 132167. https://doi.org/10.1016/J.CONBUILDMAT.2023.132167